A&A 606, A124 (2017)
DOI: 10.1051/0004-6361/201731203

Astronomy & Astrophysics

Sulphur-bearing molecules in AGB stars

I. The occurrence of hydrogen sulphide

T. Danilovich[1,⋆], M. Van de Sande[1], E. De Beck[2], L. Decin[1], H. Olofsson[2], S. Ramstedt[3], and T. J. Millar[4]

[1] Department of Physics and Astronomy, Institute of Astronomy, KU Leuven, Celestijnenlaan 200D, 3001 Leuven, Belgium
e-mail: taissa.danilovich@kuleuven.be
[2] Onsala Space Observatory, Department of Earth and Space Sciences, Chalmers University of Technology, 43992 Onsala, Sweden
[3] Department of Physics and Astronomy, Uppsala University, Box 516, 75120 Uppsala, Sweden
[4] Astrophysics Research Centre, School of Mathematics and Physics, Queen's University Belfast, University Road, Belfast BT7 1NN, UK

Received 19 May 2017 / Accepted 14 July 2017

ABSTRACT

Context. Sulphur is a relatively abundant element in the local Galaxy that is known to form a variety of molecules in the circumstellar envelopes of AGB stars. The abundances of these molecules vary based on the chemical types and mass-loss rates of AGB stars.
Aims. Through a survey of (sub-)millimetre emission lines of various sulphur-bearing molecules, we aim to determine which molecules are the primary carriers of sulphur in different types of AGB stars. In this paper, the first in a series, we investigate the occurrence of H_2S in AGB circumstellar envelopes and determine its abundance, where possible.
Methods. We surveyed 20 AGB stars with a range of mass-loss rates and different chemical types using the Atacama Pathfinder Experiment (APEX) telescope to search for rotational transition lines of five key sulphur-bearing molecules: CS, SiS, SO, SO_2, and H_2S. Here we present our results for H_2S, including detections, non-detections, and detailed radiative transfer modelling of the detected lines. We compared results based on various descriptions of the molecular excitation of H_2S and different abundance distributions, including Gaussian abundances, where possible, and two different abundance distributions derived from chemical modelling results.
Results. We detected H_2S towards five AGB stars, all of which have high mass-loss rates of $\dot{M} \geq 5 \times 10^{-6}$ $M_\odot$ yr^{-1} and are oxygen rich. H_2S was not detected towards the carbon or S-type stars that fall in a similar mass-loss range. For the stars in our sample with detections, we find peak o-H_2S abundances relative to H_2 between 4×10^{-7} and 2.5×10^{-5}.
Conclusions. Overall, we conclude that H_2S can play a significant role in oxygen-rich AGB stars with higher mass-loss rates, but is unlikely to play a key role in stars of other chemical types or in lower mass-loss rate oxygen-rich stars. For two sources, V1300 Aql and GX Mon, H_2S is most likely the dominant sulphur-bearing molecule in the circumstellar envelope.

Key words. stars: AGB and post-AGB – circumstellar matter – stars: evolution – stars: mass-loss

1. Introduction

One of the latter stages in the evolution of a low- to intermediate-mass star is the asymptotic giant branch (AGB). The AGB phase is characterised by intense mass loss through a steady stellar wind. This outflow forms a circumstellar envelope (CSE) that is rich in chemical diversity, in which molecules and dust form. The nature of the CSE is of particular interest as it contains matter that is eventually returned to the interstellar medium (ISM) and contributes to the chemical enrichment and evolution of the Galaxy. Although most molecules formed in the CSE are eventually photodissociated by photons from the interstellar UV field, some may be condensed onto dust grains and hence not introduced into the ISM in their atomic form.

Sulphur is the tenth most abundant element in the Universe and one of the essential elements for life on Earth. The molecularly rich envelopes of AGB stars are known to form molecules such as CS, SiS, SO, SO_2, and H_2S, which vary in abundance depending on chemical type and mass-loss rate. For example, CS is most abundant in carbon stars (compare the abundances found by Olofsson et al. 1993, for carbon stars and those found by Lindqvist et al. 1988 for oxygen-rich stars), and SO and SO_2 are most abundant in oxygen-rich stars (Danilovich et al. 2016). Furthermore, sulphur is not formed in AGB stars nor their main sequence progenitors, so the total amount of sulphur-bearing molecules can be constrained based on upper limits from galactic and solar abundances for sulphur. Indeed, Danilovich et al. (2016) began to do this based on a thorough study of SO and SO_2 in a small sample of M-type AGB stars.

It has been suggested that an infrared spectral feature at 30 μm may be due to MgS dust (see e.g. Goebel & Moseley 1985; Begemann et al. 1994) and may account for a significant proportion of the available sulphur in carbon-rich AGB stars. However, a more recent study by Zhang et al. (2009) found that to reproduce the 30 μm feature, a larger quantity of sulphur in the form of MgS was required than was available in circumstellar envelopes. Hence the feature is likely not due to MgS. This is further emphasised by studies of post-AGB stars, which find significant depletion of refractory elements but minimal depletion of sulphur, indicating that sulphur is not condensed onto dust in large quantities (see e.g. Waelkens et al. 1991; Reyniers & van Winckel 2007).

Chemical models that include sulphur chemistry often take SiS and H_2S to be the parent species, i.e. the molecules in

⋆ Postdoctoral Fellow of the Fund for Scientific Research (FWO), Flanders, Belgium.

which sulphur is initially contained at the model inner radius (Willacy & Millar 1997; Cherchneff 2006, 2012; Agúndez et al. 2010; Li et al. 2016), especially for oxygen-rich stars. However, the specific choice of parent species and their initial abundances can lead to different outcomes in chemical modelling (Li et al. 2016), including differences in the shape and peak values of various abundance distributions in the CSE. Varying approaches to chemical modelling also give different results. For example, Willacy & Millar (1997) considered the photo-dominated low-density outer part of the CSE, at radii $>10^{15}$ cm for oxygen-rich stars and, having assumed H_2S to be the key S-bearing parent species, they predicted a consistent decline in H_2S abundance as it reacts to form other S-bearing species such as CS, SO and SO_2. Li et al. (2016) have considered a similar region of an oxygen-rich CSE, but have assumed a much lower inner H_2S abundance – in their model the majority of the sulphur is initially found in SiS – and have found a slight increase in H_2S before it decreases at a similar rate to the Willacy & Millar (1997) models. The models of Agúndez et al. (2010) considered a clumpy CSE medium for a range of mass-loss rates through which UV photons are potentially able to penetrate to the inner regions. Their models of carbon stars, which include inner regions close to the dust condensation region and outer regions comparable to the Willacy & Millar (1997) and Li et al. (2016) models, found rapid formation of H_2S followed by two stages of destruction, first rapid then more moderate, for carbon-rich CSEs (their H_2S results for oxygen-rich CSEs not shown). Gobrecht et al. (2016) have studied the innermost regions of an oxygen-rich CSE, closest to the AGB star itself and within the dust condensation region, examining the effects of shocks on molecular abundances and dust condensation. They have found a high abundance of H_2S close to the star, which drops off rapidly as H_2S is destroyed by various chemical processes.

H_2S is not commonly detected in AGB stars other than the high mass-loss rate OH/IR stars ($\dot{M} \sim 10^{-4}$ $M_\odot$ yr^{-1}). For example, the *Herschel*/HIFI Guaranteed Time Key Project HIFISTARS observed the H_2S ($3_{1,2} \rightarrow 2_{2,1}$) line at 1196.012 GHz in nine M-type AGB stars, but only detected this line in AFGL 5379, which has been classified as an OH/IR star (Justtanont et al. 2012). Justtanont et al. (2015) detected several H_2S lines in all eight of the OH/IR stars they observed with *Herschel*/SPIRE and *Herschel*/PACS. Ukita & Morris (1983) searched for the H_2S ($1_{1,0} \rightarrow 1_{0,1}$) line at 168.763 GHz in 25 AGB sources and detected it only in OH 231.8 +4.2 (aka the Rotten Egg Nebula), an OH/IR star that may be transitioning to the post-AGB phase. Omont et al. (1993) surveyed a diverse sample of evolved stars for several sulphur-bearing molecules and detected H_2S in 15 sources, including high mass-loss rate AGB stars and OH/IR stars. The sources in which these authors did not detect H_2S include carbon stars, S-type stars, and lower mass-loss rate M-type AGB stars. Albeit, they also confirmed the detection of H_2S in CW Leo, which is the only carbon star for which H_2S has been detected to date with detections from several studies of the 168 GHz ortho-H_2S line (Cernicharo et al. 1987, 2000; Omont et al. 1993). However, the para-H_2S ($2_{2,0} \rightarrow 2_{1,1}$) line at 216.710 GHz has not been detected in CW Leo (see e.g. the Tenenbaum et al. 2010, 1 mm survey), nor has the ortho-H_2S ($3_{3,0} \rightarrow 3_{2,1}$) line at 300.506 GHz (see e.g. the Patel et al. 2011 survey).

To better constrain the abundances and distributions of the most abundant sulphur-bearing molecules in AGB stars of different chemical types and a range of mass-loss rates, we performed a survey of H_2S, SiS, CS, SO, and SO_2 with the Atacama Pathfinder Experiment (APEX[1]), a 12 m radio telescope located at Llano Chajnantor in northern Chile. In this series of papers we intend to investigate the occurrence and abundance distributions of these key sulphur-bearing molecules. Once the abundances are known we intend to conduct a detailed chemical analysis of S-bearing species, including detailed chemical modelling. In this first study, we present results of the H_2S observations from this survey.

2. Sample and observations

2.1. APEX survey

We observed several lines of CS, SiS, SO, SO_2, and H_2S in a diverse sample of 20 AGB stars, including 7 M-type stars, 5 S-type stars, and 8 carbon stars and covering mass-loss rates from $\sim 9 \times 10^{-8}$ $M_\odot$ yr^{-1} to $\sim 2 \times 10^{-5}$ $M_\odot$ yr^{-1}. The sample was chosen to cover a range of mass-loss rates across all three chemical types and was largely drawn from stars covered by the SUCCESS programme (Danilovich et al. 2015), for which high quality CO observations and mass-loss rates derived from CO modelling were already available. Of this sample all but two sources were observed for at least one of three possible H_2S transitions and H_2S was detected in three of these sources. To expand our sample, an additional three high mass-loss rate M-type sources were added and observed only in the frequency setting containing the H_2S line at 168.763 GHz. H_2S was detected in two of these sources.

Observations were carried out using the Swedish-ESO PI receiver for APEX (SEPIA Band 5, Billade et al. 2012) and the Swedish Heterodyne Facility Instrument (SHeFI; Risacher et al. 2006; Vassilev et al. 2008). The data were reduced via the GILDAS/CLASS[2] software package. Following the initial assessment by Immer et al. (2016) of the performance of SEPIA, we assumed a main beam efficiency of $\eta_{\rm mb} = 0.68$ for our SEPIA tunings. The well-established main beam efficiencies of $\eta_{\rm mb} = 0.75$ and $\eta_{\rm mb} = 0.73$ (Güsten et al. 2006) were used for the 216 GHz and 300 GHz observations, respectively. The beam sizes corresponding to each transition are listed in Table 2 and the emission is spatially unresolved for all lines observed with APEX.

The full sample of stars included in the APEX H_2S survey is listed in Table 1. The lines included in the survey are listed in Table 2, along with other available lines from other telescopes. Table 3 includes all the detected H_2S lines and their integrated main beam intensities and Table 4 lists all the observed sources with the root mean square (RMS) noise limit at 1 km s^{-1} for each observed line. We list all non-detections for completion.

We encountered no issues with line ambiguity for the 168 GHz and 300 GHz lines; there were no plausible alternative identifications for these lines. The 216 GHz line, which was only tentatively detected in IK Tau could potentially be an overlap with ^{13}CN. However, the ^{13}CN features around 216 GHz are weak and not even detected in the two carbon stars for which other ^{13}CN groups are seen at around 217 GHz and 218 GHz. Hence, we conclude that the weak emission seen at 216.710 GHz towards IK Tau is most likely due to H_2S.

Of the three H_2S lines observed as part of this project, the ortho-H_2S ($1_{1,0} \rightarrow 1_{0,1}$) line was the brightest and most likely

[1] This publication is based on data acquired with the Atacama Pathfinder Experiment (APEX). APEX is a collaboration between the Max-Planck-Institut für Radioastronomie, the European Southern Observatory, and the Onsala Space Observatory.
[2] http://www.iram.fr/IRAMFR/GILDAS/

Table 1. Basic parameters of surveyed stars.

Star	RA	Dec	$\upsilon_{\rm LSR}$ [km s^{-1}]	Distance [pc]	$\dot{M}$ [$M_\odot$ yr^{-1}]	$T_{\rm eff}$ [K]	υ_∞ [km s^{-1}]	Ref.
M-type stars								
R Hor	02:53:52.77	−49:53:22.7	37	310	5.9×10^{-7}	2200	4	1
IK Tau	03:53:28.87	+11:24:21.7	34	265	5.0×10^{-6}	2100	17.5	2
GX Mon	06:52:46.91	+08:25:19.0	−9	550	8.4×10^{-6}	2600	19	1
W Hya	13:49:02.00	−28:22:03.5	40.5	78	1.0×10^{-7}	2500	7.5	3
RR Aql	19:57:36.06	−01:53:11.3	28	530	2.3×10^{-6}	2000	9	1
V1943 Sgr	20:06:55.24	−27:13:29.8	−15	200	9.9×10^{-8}	2200	6.5	1
V1300 Aql	20:10:27.87	−06:16:13.6	−18	620	1.0×10^{-5}	2000	14	1
V1111 Oph	18:37:19.26	+10:25:42.2	−32	750	1.2×10^{-5}	2000	17	1
WX Psc	01:06:25.98	+12:35:53.1	9.5	700	4.0×10^{-5}	1800	19	5
IRC-30398	18:59:13.85	−29:50:20.4	−6.5	550	8.0×10^{-6}	1800	16	5
S-type stars								
T Cet	00:21:46.27	−20:03:28.9	22	240	6.0×10^{-8}	2400	7	5
TT Cen	13:19:35.02	−60:46:46.3	4	880	4.0×10^{-6}	1900	20	5
W Aql	19:15:23.35	−07:02:50.4	−23	395	4.0×10^{-6}	2300	16.5	4
RZ Sgr	20:15:28.41	−44:24:37.5	−31	730	3.0×10^{-6}	2400	9	6
Carbon stars								
R Lep	04:59:36.35	−14:48:22.5	11	432	8.7×10^{-7}	2200	18	1
V1259 Ori	06:03:59.84	+07:25:54.4	42	1600	8.8×10^{-6}	2200	16	1
AI Vol	07:45:02.80	−71:19:43.2	−39	710	4.9×10^{-6}	2100	12	1
X TrA	15:14:19.18	−70:04:46.1	−2	360	1.9×10^{-7}	2200	6.5	1
II Lup	15:23:04.91	−51:25:59.0	−15.5	500	1.7×10^{-5}	2400	21.5	1
V821 Her	18:41:54.39	+17:41:08.5	−0.5	600	3.0×10^{-6}	2200	13.5	1
RV Aqr	21:05:51.68	−00:12:40.3	1	670	2.3×10^{-6}	2200	15	1

Notes. References give details of mass-loss rate, $\dot{M}$, stellar effective temperature, $T_{\rm eff}$, and distances. (1) Danilovich et al. (2015); (2) Maercker et al. (2016); (3) Khouri et al. (2014) and Danilovich et al. (2016); (4) Danilovich et al. (2014); (5) Ramstedt & Olofsson (2014); (6) Schöier et al. (2013).

Table 2. Observed transitions.

Line	Frequency [GHz]	Telescope	θ [″]
o-H_2S ($1_{1,0} \rightarrow 1_{0,1}$)	168.763	APEX	37
p-H_2S ($2_{2,0} \rightarrow 2_{1,1}$)	216.710	APEX	29
o-H_2S ($3_{3,0} \rightarrow 3_{2,1}$)	300.506	APEX	21
		SMA	1
o-H_2S ($3_{1,2} \rightarrow 2_{2,1}$)	1196.012	HIFI	19.5
o-$H_2{}^{34}S$ ($1_{1,0} \rightarrow 1_{0,1}$)	167.911	APEX	37

Notes. θ is the HPBW.

to be detected of the three H_2S lines observed. Hence, we determined that a non-detection of the ($1_{1,0} \rightarrow 1_{0,1}$) line places a firmer upper limit on the possible H_2S abundance in each source than a non-detection of either the para-H_2S ($2_{2,0} \rightarrow 2_{1,1}$) line or the ortho-$H_2S$ ($3_{3,0} \rightarrow 3_{2,1}$), both of which were, at best, only tentatively detected in the sources that had clear ($1_{1,0} \rightarrow 1_{0,1}$) detections.

A first-order approximation for expected relative integrated line intensities between various stars is given by the mass-loss rate divided by the square of the distance, since integrated line intensity is generally expected to increase with mass-loss rate (neglecting specific abundances and optical depth effects) and decrease with the inverse square of the distance. In Fig. 1 this quantity, $\dot{M}/D^2$, is plotted against the mass-loss rate, $\dot{M}$, for all observed sources. As can be clearly seen, the sources for which H_2S has been detected all have high mass-loss rates and are expected to exhibit bright emission lines. However, H_2S was seen only in the M-type stars and not, for example, in the bright, high mass-loss rate carbon star II Lup nor in the slightly less bright and slightly lower mass-loss rate S-type star W Aql. The only non-M-type AGB star for which H_2S has been detected to date is CW Leo, which has a similar mass-loss rate to II Lup and, because of its proximity, a brightness of 1.4×10^{-9} $M_\odot$ yr^{-1} pc^{-2}, putting it outside of our axes in Fig. 1. We also distinguished the non-detections with different markers depending on which lines were observed for each source and hence the strength of the upper limit constraints that we can place on H_2S abundances. The filled markers indicate a non-detection of the strong ($1_{1,0} \rightarrow 1_{0,1}$) line, while the unfilled markers indicate the non-detection of the ($2_{2,0} \rightarrow 2_{1,1}$) and ($3_{3,0} \rightarrow 3_{2,1}$) line in the absence of observations of the much brighter ($1_{1,0} \rightarrow 1_{0,1}$) lines.

In addition to the three targeted $H_2{}^{32}S$ lines, we concurrently observed the $H_2{}^{34}S$ ($1_{1,0} \rightarrow 1_{0,1}$) line at 168.911 GHz and detected it in WX Psc and, tentatively, in V1300 Aql. All detected H_2S lines are plotted in Fig. 2 at a velocity resolution of 2 km s^{-1}, for the noisiest detections, or 1 km s^{-1} for the clearer detections.

2.2. Supplementary observations

The ($3_{3,0} \rightarrow 3_{2,1}$) o-$H_2S$ transition at 300.506 GHz was observed towards IK Tau as part of an unbiased survey in the 279–355 GHz range using the Submillimeter Array (SMA) in the extended configuration. The full details of this survey are given

Table 3. Main beam integrated intensities for detections from APEX survey.

Star	H_2S $1_{1,0} \rightarrow 1_{0,1}$ [K km s^{-1}]	H_2S $2_{2,0} \rightarrow 2_{1,1}$ [K km s^{-1}]	H_2S $3_{3,0} \rightarrow 3_{2,1}$ [K km s^{-1}]	$H_2{}^{34}S$ $1_{1,0} \rightarrow 1_{0,1}$ [K km s^{-1}]
IK Tau	1.85	0.26:	x	x
GX Mon	1.07	x	x	x
V1300 Aql	1.50	x	0.26:	0.34:
V1111 Oph	0.79	...	...	x
WX Psc	2.46	...	...	0.55

Notes. (:) indicates a tentative detection; x indicates a non-detection (see Table 4 for RMS); (...) indicates lines that were not observed.

Table 4. RMS noise for all observed H_2S lines from APEX survey.

Star	H_2S $1_{1,0} \rightarrow 1_{0,1}$	H_2S $2_{2,0} \rightarrow 2_{1,1}$	H_2S $3_{3,0} \rightarrow 3_{2,1}$	$H_2{}^{34}S$ $1_{1,0} \rightarrow 1_{0,1}$
M-type stars				
R Hor	11	...	13	11
IK Tau	18^{D}	17^{T}	20	18
GX Mon	20^{D}	12	18	20
W Hya	16	...	11	16
RR Aql	19	15	13	19
V1943 Sgr	13	...	11	13
V1300 Aql	13^{D}	20	15^{T}	13^{T}
V1111 Oph	13^{D}	...	...	13
WX Psc	8^{D}	...	...	8^{D}
IRC-30398	13	...	...	13
S-type stars				
T Cet	...	13	...	...
TT Cen	20	...	10	20
W Aql	13	14	14	13
RZ Sgr	20	...	13	20
Carbon stars				
R Lep	...	16	...	...
V1259 Ori	17	14	15	17
AI Vol	20	17	...	20
X TrA	...	13	...	...
II Lup	10*	11	10	...
V821 Her	19	18	...	19
RV Aqr	...	15	...	...

Notes. RMS values given in mK at a velocity resolution of 1 km s^{-1}. (...) indicates lines that were not observed, (^{D}) and (^{T}) indicate detected or tentatively detected lines, respectively (see Table 3 for integrated intensities). (*) indicates that the APEX observation is from De Beck et al. (in prep.).

in De Beck et al. (2013). The size of the synthetic beam at this frequency was $0.95'' \times 0.93''$ and the H_2S emission was not resolved. For our study, the emission line of interest was extracted for a synthetic circular beam $1''$ in diameter and is used to constrain our models.

IK Tau and WX Psc (aka IRC+10011) were observed with *Herschel*/HIFI as part of the HIFISTARS Guaranteed Time Key Project (de Graauw et al. 2010; Bujarrabal et al. 2011; Roelfsema et al. 2012). The o-H_2S ($3_{1,2} \rightarrow 2_{2,1}$) line at 1196.012 GHz was observed as part of this project but not detected in either of the two sources in our sample (Justtanont et al. 2012). However, we use the non-detections as upper limits to help constrain our models. We re-reduced the data using the *Herschel* interactive processing environment (HIPE[3] version 14.2.1, Ott 2010) and the updated main beam efficiencies of Mueller et al. (2014)[4], which were released subsequent to the Justtanont et al. (2012) publication.

3. Modelling

3.1. Established parameters

Most of the stars in our survey were chosen from the sample presented in Danilovich et al. (2015). In that study, a large sample of AGB stars were observed across several CO emission lines and radiative transfer analyses were performed to determine circumstellar parameters based on the CO emission. Our circumstellar models are based on the results found in that paper. For WX Psc,

[3] http://www.cosmos.esa.int/web/herschel/data-processing-overview

[4] http://herschel.esac.esa.int/twiki/pub/Public/HifiCalibrationWeb/HifiBeamReleaseNote_Sep2014.pdf

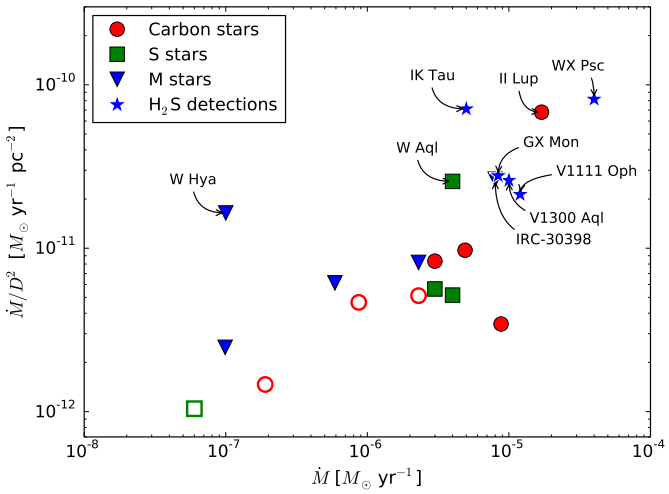

Fig. 1. Predictor of integrated line brightness, $\dot{M}/D^2$, plotted against mass-loss rate for our sample. Marker types denote which observed H_2S lines were undetected. Filled markers indicate that ($1_{1,0} \rightarrow 1_{0,1}$) was undetected, as were the other two lines if they were observed. Unfilled markers indicate that ($2_{2,0} \rightarrow 2_{1,1}$) was undetected and that the brighter ($1_{1,0} \rightarrow 1_{0,1}$) and ($3_{3,0} \rightarrow 3_{2,1}$) were not observed.

which was not included in Danilovich et al. (2015), we used the circumstellar model results from Ramstedt & Olofsson (2014) and Danilovich et al. (in prep.), and for IK Tau we used the results from Maercker et al. (2016), all of which were obtained via the same Monte Carlo method used by Danilovich et al. (2015), ensuring homogeneity. This modelling method was first described in detail by Schöier & Olofsson (2001) and its reliability was detailed by Ramstedt et al. (2008), who note uncertainties up to a factor of ~3. Danilovich et al. (2015) have also compared their results with past studies and have concluded that on average they find mass-loss rates 40% lower than past studies, most likely due to the modelling of an acceleration region and their inclusion of relatively high-J CO lines. Some of the key circumstellar parameters for our sample – LSR velocity, $\upsilon_{\rm LSR}$, distance, and mass-loss rate, $\dot{M}$ – are listed in Table 1.

For the radiative transfer analysis we treated ortho- and para-H_2S separately since there are no gas-phase transitions linking the two spin isomers. We tested two molecular data files. The first included only the ground vibrational state and collisional rates taken from Dubernet et al. (2009), which were obtained from the LAMDA[5] database (Schöier et al. 2005) and that we henceforth refer to as the LAMDA description. The second data file is more comprehensive, including vibrationally excited energy levels and collisional rates from Faure et al. (2007), which we will refer to as the JHB description. The LAMDA description comprises 45 energy levels each for ortho- and para-H_2S and 139 and 140 radiative transitions for ortho- and para-H_2S, respectively; these are all taken from the JPL[6] spectroscopic database (Pickett et al. 1998). The collisional rates, which cover 990 collisional transitions for each of ortho- and para-H_2S at temperatures ranging from 5 to 1500 K, are scaled from the H_2O rates from Dubernet et al. (2009) and assume an H_2 ortho-to-para ratio (OPR) of 3. The JHB molecular data file contains 243 and 247 energy levels for ortho- and para-H_2S, respectively, with levels with energies up to approximately 6000 K. Levels included are rotational energy levels in the ground vibrational state up to $J_{K_a,K_c} = 12_{4,9}$ (ortho) and $J_{K_a,K_c} = 12_{3,9}$ (para), and levels in the $(\nu_1, \nu_2, \nu_3) = (0, 1, 0), (0, 2, 0), (0, 3, 0), (1, 0, 0), (0, 0, 1), (1, 1, 0), (0, 1, 1)$ vibrationally excited states up to and including all rotational levels with $J = 6$. The molecular data file also includes 1084 and 1039 radiative transitions for ortho- and para-H_2S, respectively, with all spectroscopic data taken from the HITRAN database (Rothman et al. 2009). The collisional rates cover temperatures from 20 to 2000 K and are scaled from the H_2O rates of Faure et al. (2007) and assume an H_2 OPR of 3. These rates cover energy levels from the ground state up to approximately 1000 K. In Fig. 3 we plot all ground state rotational energy levels up to $J = 6$ for both ortho- and para-H_2S.

[5] http://home.strw.leidenuniv.nl/~moldata/
[6] https://spec.jpl.nasa.gov

3.2. Radiative transfer modelling procedure

Based on the circumstellar parameters and molecular data files discussed above, we performed detailed radiative transfer modelling of the H_2S emission in our sources using an accelerated lambda iteration method code (ALI). The ALI code has been previously described in detail by Maercker et al. (2008) and Schöier et al. (2011) and has been implemented to model molecular emission from a wide variety of molecules in those studies and in Danilovich et al. (2014, 2016). Our models assume a smoothly accelerating and spherically symmetric CSE created by mass lost at a constant rate by the central AGB star. We assume H_2S abundance distributions based on chemical model results and on radial Gaussian profiles.

In the cases where more than one H_2S line was observed, we assume a Gaussian fractional abundance distribution of H_2S, centred on the star and described by

$$f(r) = f_0 \exp\left(-\left(\frac{r}{R_e}\right)^2\right), \quad (1)$$

where f_0 is the peak central abundance and R_e is the e-folding radius at which the abundance has dropped to f_0/e. As we have no a priori constraints on the e-folding radius, we leave both f_0 and R_e as free parameters in our modelling to be adjusted to best fit the available data. Since we have some sources with only one H_2S line detected, we cannot properly constrain a Gaussian profile for those sources (see further discussion in Sect. 4.2). In those cases we only use abundance distributions derived from chemical modelling (described further in Sect. 3.3) that are scaled to fit our observations.

In general we attempted to run our models using both the LAMDA and JHB molecular data files. We also extracted just the ground state information from the JHB description to create the GS JHB description and to allow us to directly compare the impact of the vibrationally excited states on the excitation analysis of H_2S. Such a direct comparison cannot be performed by comparing the full JHB file with the LAMDA file as there may be additional variations introduced by the different collisional rates used in the two files.

Owing to the uncertainty in the choice of molecular data file, we did not model our observations of para-H_2S, which was only tentatively detected towards IK Tau, or $H_2{}^{34}S$, which was detected towards WX Psc and tentatively detected towards V1300 Aql. The uncertainty in our o-$H_2{}^{32}S$ models (discussed in further detail below) is such that any comparisons would not be meaningful at present. A direct comparison of $H_2{}^{34}S$ with $H_2{}^{32}S$ based on line strengths is also not possible since the $H_2{}^{32}S$ ($1_{1,0} \rightarrow 1_{0,1}$) line is optically thick for both V1300 Aql and WX Psc. Clearer and more numerous observations of p-H_2S and $H_2{}^{34}S$ would facilitate a more comprehensive and significant comparison.

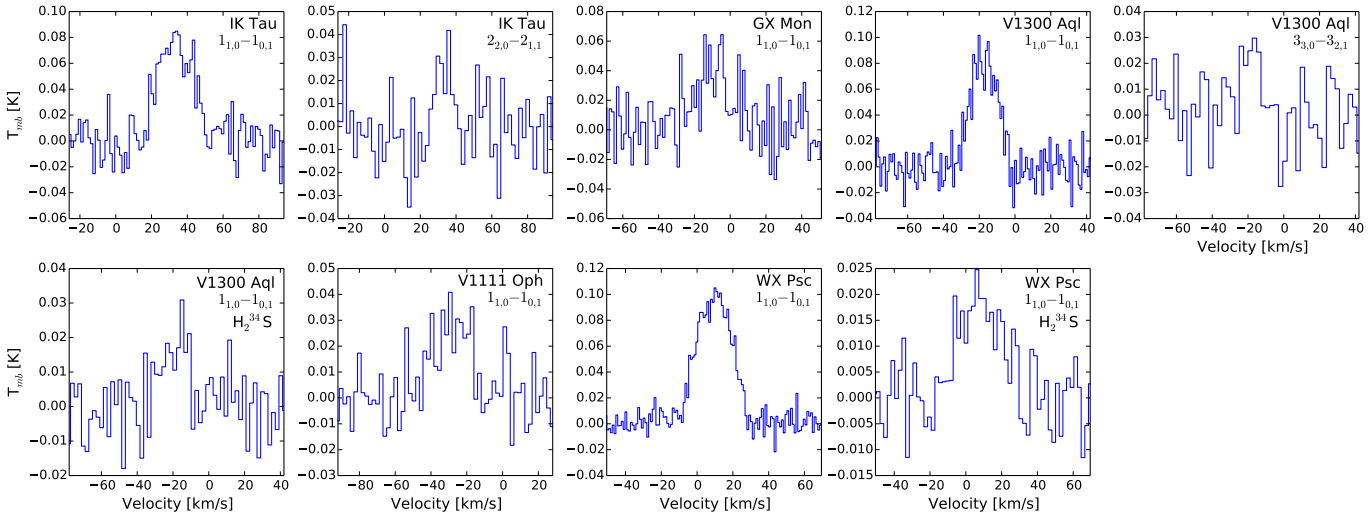

Fig. 2. All detections and tentative detections of H_2S and $H_2{}^{34}S$ lines from our APEX survey. All lines are marked with their transition (see Table 2 for frequencies). Observations of $H_2{}^{34}S$ lines are indicated below the transition numbers and all other lines are of $H_2{}^{32}S$.

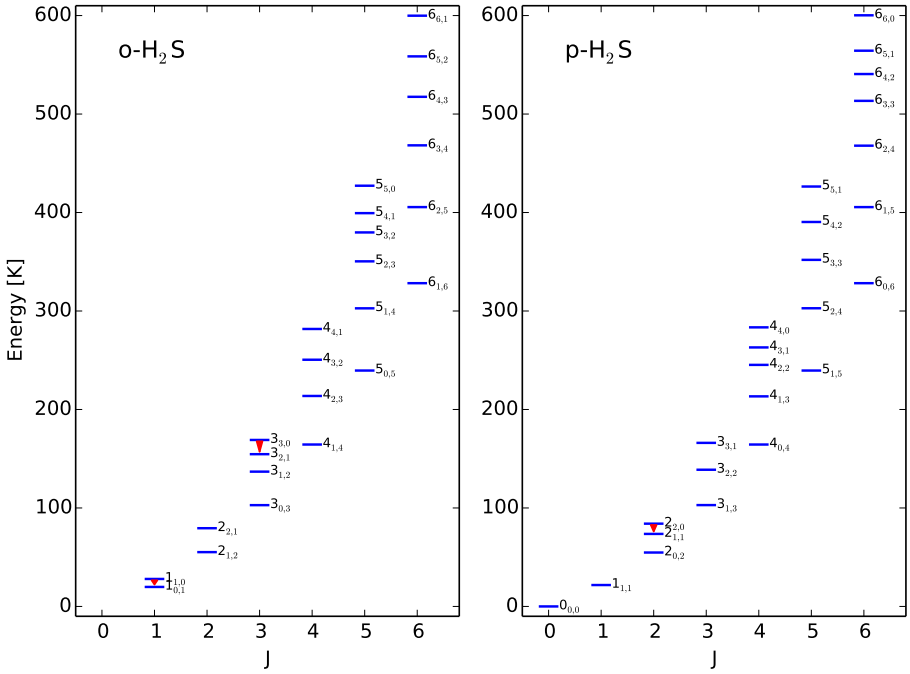

Fig. 3. Energy level diagram for H_2S with ortho energy levels shown on the left and para energy levels shown on the right. The quantum numbers are listed to the right of each level in the format J_{K_a,K_c}. The red wedges indicate the transitions observed by APEX as part of this study.

3.3. Chemical modelling

To put an additional constraint on the abundance distribution of H_2S for each of our stars, we derived abundance distributions from chemical modelling. The forward chemistry model used is based on the UMIST Database for Astrochemistry (UDfA) CSE model. The chemical reaction network used is the most recent release of UDfA, RATE12 (McElroy et al. 2013). The network includes only gas-phase reactions with a total of 6173 reactions involving 467 species. Both the UDfA CSE model and RATE12 are publicly available[7].

The one-dimensional model assumes a uniformly expanding and spherically symmetric outflow, with both a constant mass-loss rate and expansion velocity, which are taken from the values listed in Table 1. Self-shielding of CO is taken into account. A more detailed description can be found in Millar et al. (2000), Cordiner & Millar (2009), and McElroy et al. (2013).

[7] http://udfa.ajmarkwick.net/index.php?mode=downloads

We changed the kinetic temperature structure of the outflow to a power law

$$T(r) = T_* \left(\frac{R_*}{r}\right)^{-\epsilon}, \quad (2)$$

with $T_* = 2000$ K, the stellar temperature, $R_* = 5 \times 10^{13}$ cm, the stellar radius, and $\epsilon = 0.65$, the exponent characterising the power law. In order to prevent unrealistically low temperatures in the outer CSE, the temperature has a set lower limit of 10 K (Cordiner & Millar 2009).

The initial abundance of all species is assumed to be zero, except for that of the parent species. The parent species are injected into the outflow at the start of the model at 1×10^{14} cm. We calculated models using two lists of parent species: the O-rich list of Agúndez et al. (2010) and the IK Tau-specific list of Li et al. (2016), both based on observational constraints where available and supplemented with thermal equilibrium calculations. These

Table 5. Modelling results for o-H_2S.

	LAMDA	JHB	GS JHB
IK Tau			
L scale:	36	48	51
f_{peak}	1.1×10^{-6}	1.7×10^{-6}	1.9×10^{-6}
A scale:	19	23	25
f_{peak}	1.1×10^{-6}	1.6×10^{-6}	1.8×10^{-6}
Gaussian: f_0	1.5×10^{-6}	1.5×10^{-6}	1.6×10^{-6}
R_e [cm]	7.7×10^{15}	3.4×10^{16}	3.4×10^{16}
GX Mon			
L scale:	36	300	410
f_{peak}	1.4×10^{-6}	1.2×10^{-5}	1.6×10^{-5}
A scale:	21	180	250
f_{peak}	1.5×10^{-6}	1.3×10^{-5}	1.8×10^{-5}
V1300 Aql			
L scale:	74	550	800
f_{peak}	3.3×10^{-6}	2.5×10^{-5}	3.6×10^{-5}
A scale:	48	360	380
f_{peak}	3.4×10^{-6}	2.5×10^{-5}	2.7×10^{-5}
Gaussian: f_0	3.4×10^{-5}	1.7×10^{-5}	2.7×10^{-5}
R_e [cm]	4.2×10^{15}	2.3×10^{16}	2.3×10^{16}
V1111 Oph			
L scale:	22	72	77
f_{peak}	9.4×10^{-7}	3.1×10^{-6}	3.3×10^{-6}
A scale:	14	49	52
f_{peak}	9.8×10^{-7}	3.4×10^{-6}	3.6×10^{-6}
WX Psc			
L scale:	12	24	26
f_{peak}	7.1×10^{-7}	1.4×10^{-6}	1.5×10^{-6}
A scale:	9.2	18	19
f_{peak}	6.4×10^{-7}	1.3×10^{-6}	1.3×10^{-6}

Notes. f_0 is the peak abundance relative to H_2 and R_e is the e-folding radius. The scales for Li and Agundez refer to the multiplicative scale factor required to fit the abundance distributions produced from chemical models using the L and A parent molecules, respectively, and f_{peak} is the peak abundance relative to H_2 after scaling those abundance distributions. See text for further details.

two model results are henceforth referred to as the A and L abundance distributions after the sources of the parent species lists.

Inputting these abundance distributions as calculated into our radiative transfer models resulted in severe under-predictions for all our observed H_2S lines. To tune these models so that they agreed with the observations, we scaled the derived abundance distributions until we found a model that best fit the data. This approach is justified since we found that increasing the initial (parent) abundance of H_2S in the forward chemistry models had the effect of increasing the abundance distribution by a uniform scale factor.

3.4. Modelling results

For each source we have found best-fit models for each of the L and A radial abundance distributions coupled with each of the available molecular data files: LAMDA, JHB, and GS JHB. This gives six models for each source. In addition, for IK Tau and V1300 Aql, the sources with multiple detections, we also found three best-fit models for a Gaussian abundance distribution paired with each of the molecular data files.

The derived abundances and radii for our sources are listed in Table 5 and the abundance distributions that best match our data (either scaled from chemical models or derived Gaussian abundance profiles) are plotted in Fig. 4. The model results for V1300 Aql and IK Tau are plotted in Fig. 5. These two stars were chosen as examples because they are the only two for which we have two detected lines (and additionally two undetected lines for IK Tau), and hence were the only two stars for which we could calculate models with Gaussian abundance distributions. In Fig. 5 we show six different variations on the choice of the abundance distribution and molecular excitation file. For V1300 Aql, for which there is a strong detection of the ($1_{1,0} \rightarrow 1_{0,1}$) line and a tentative detection of the ($3_{3,0} \rightarrow 3_{2,1}$) line, the models are most strongly constrained by the stronger line, since the weaker line has a larger uncertainty. This is particularly evident when considering that all the models fit the ($1_{1,0} \rightarrow 1_{0,1}$) line equally well, whereas the two models with chemically modelled abundances paired with the LAMDA molecular data file predict much weaker ($3_{3,0} \rightarrow 3_{2,1}$) emission than the other four models. From this we can conclude that, for V1300 Aql, the models with fixed abundance distributions – which are similar in radial size to the Gaussian distribution we find for the JHB molecular data file – do not give realistic results when paired with the LAMDA molecular data file. This effect is more pronounced for V1300 Aql than for IK Tau, for which we find generally lower o-H_2S abundances.

Overall, as can be seen in Table 5 and Figs. 4 and 5, the different molecular data files give varying results – most notably different peak abundances – when other factors such as the abundance distribution were held constant. Conversely, changing the abundance distribution induced less significant differences in peak abundances when the molecular data files were held constant. These effects are discussed in more detail in Sects. 4.1 and 4.2. We have not included formal uncertainties for our models since these are much smaller than the difficult-to-quantify errors introduced by the choice of collisional rates.

4. Discussion

4.1. The choice of molecular excitation data

In examining the results of using various molecular data files, we determined that the most significant difference was not in the inclusion or not of vibrationally excited states – although this played a small role as can be seen when comparing the results of the JHB description and the GS JHB description – but in the choice of collisional rates. Also, both molecular data files only include collisional rates for transitions in the ground vibrational state.

The LAMDA file includes collisional rates based on those determined by Dubernet et al. (2006, 2009) and Daniel et al. (2010, 2011) for H_2O collisions with p-H_2 and o-H_2, scaled to the mass of H_2S. The JHB file includes collisional rates based on the H_2O rates calculated by Faure et al. (2007), which are based on quasi-classical trajectory calculations and are most suited to high-temperature situations. Indeed, when discussing H_2O, Dubernet et al. (2009) recommend the use of the Faure et al. (2007) collisional coefficients for high temperatures above 400 K; Dubernet et al. caution that the weakest transitions included by Faure et al. (2007) are based on scaled H_2O-He collisions, which are the least accurate. Below 400 K, Dubernet et al. (2009) and Daniel et al. (2011) recommend the use of their own collisional rates. However, the temperatures within AGB CSEs range from cool (~10 K) to warm (~2000 K), spanning both sides of the suggested 400 K cutoff. The review of van der Tak (2011) suggests that for H_2O the collisional rates of

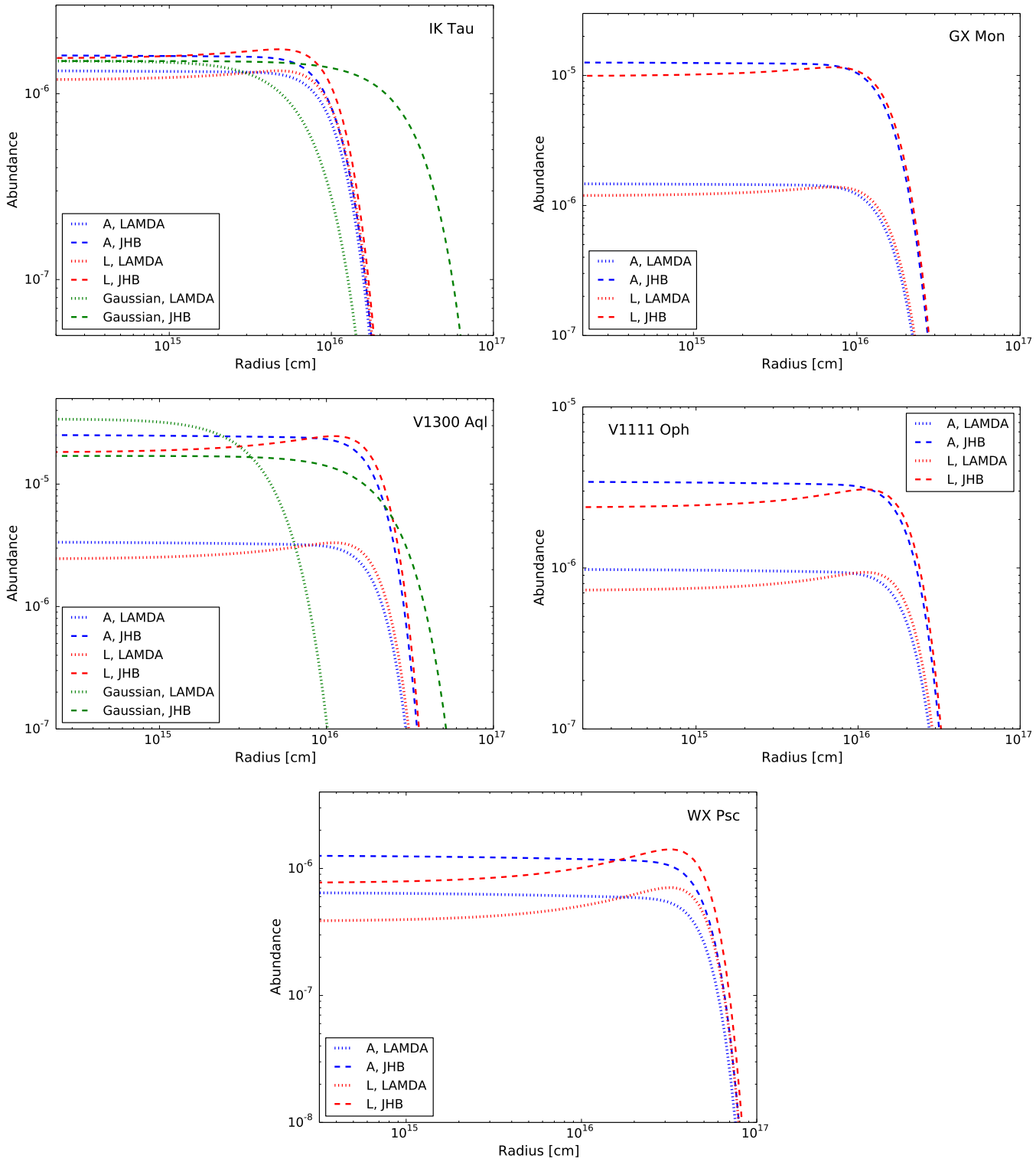

Fig. 4. Abundance distributions, o-H_2S/H_2, that best fit our data with different molecular data files. Dotted lines represent models using the LAMDA molecular data file; dashed lines represent models using the JHB molecular data file. Blue curves are abundance distributions based on chemical models arising from parent molecule list A, red curves similarly arise from parent molecule list L, and green curves are Gaussian abundance distributions.

Dubernet et al. (2006) are the best collisional rates to use for low temperatures (≤20 K, such as found in some molecular clouds). At warm temperatures (~300 K), however, the best collisional rates are those from Faure et al. (2007); at high temperatures (≥300 K) the collisional rates from Faure & Josselin (2008), which include vibrational excitation, are preferred. This does not, however, avoid the problem of AGB CSEs spanning all three temperature regimes.

One of the key problems here is that the precise correspondence of the H_2O rates to the H_2S rates is not presently known.

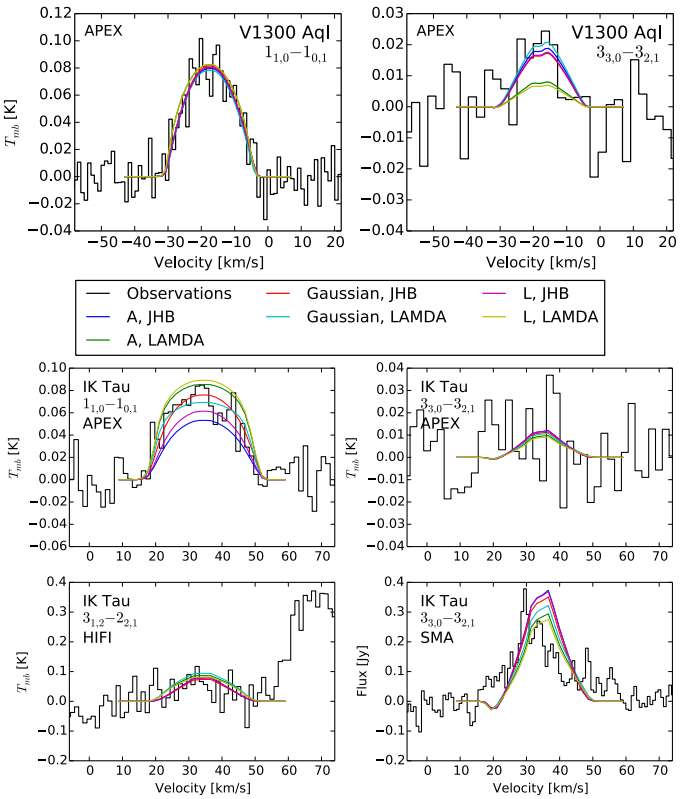

Fig. 5. Observations and model lines for o-H_2S towards V1300 Aql (*top*) and IK Tau (*bottom*). Different coloured curves indicate the results of best-fit models derived using various methods described in the text.

Merely scaling to account for the different masses of H_2O and H_2S does not take into account differences in molecular cross-section and dipole moments. Furthermore, Daniel et al. (2011) note that the H_2O-H_2 rates obtained by scaling rates from H_2O-He (such as those by Green et al. 1993) are the least reliable. There is no similar data on the reliability of scaling H_2O-H_2 rates to H_2S-H_2 rates, which may be significant, given that the dipole moments of the two molecules differ by a factor of ~2 (1.8546 D for H_2O, Lide 2003; and 0.974 D for H_2S, Viswanathan & Dyke 1984).

Another issue when deriving H_2S collisional rates from H_2O collisional rates is that the distribution of energy levels for H_2S is not perfectly analogous to that of H_2O. For the JHB molecular data file these subtleties are taken into consideration, whereas for the LAMDA description they are not; therefore, for some transitions the de-excitation rate is instead listed as the excitation rate because of a reversed energy order with respect to the H_2O levels, which slightly alters the model.

To further quantify the dependence of H_2S on the choice of collisional rates, we scaled the collisional rates given in both the JHB and LAMDA files by several factors up to two orders of magnitudes in both increasing and decreasing directions. All rates were scaled uniformly and the resulting comparison was made for the modelled integrated intensity for four o-H_2S transition lines that are the three key lines from our various observations: ($1_{1,0} \rightarrow 1_{0,1}$), ($3_{3,0} \rightarrow 3_{2,1}$), and ($3_{1,2} \rightarrow 2_{2,1}$), and a higher-$J$ line at 407.677 GHz ($5_{4,1} \rightarrow 5_{3,2}$). For these test models we used the basic parameters for V1111 Oph as listed in Table 1 and Sect. 3. We assumed a Gaussian H_2S distribution with an inner H_2S abundance of 1×10^{-6} and an e-folding radius of 1×10^{16} cm. The results, showing the variation in integrated line intensity with collisional rate scale factor, are plotted in Fig. 6. Varying the collisional rates as we have done has a significant impact on the resulting integrated line intensities. This strongly suggests that H_2S is primarily collisionally excited rather than radiatively excited, and hence that the choice of collisional rates is important to precisely constrain its abundance and distribution in a CSE. The choice of collisional rates appears to have a larger impact than the smaller range of energy levels and radiative transitions included in the LAMDA file compared with the JHB file. Similar tests of collisional rates for SO_2 resulted in very minor changes in integrated line intensities, implying that SO_2 is instead primarily radiatively excited (Danilovich et al. 2016). Unlike for SO_2, the importance of the collisional rates for H_2S indicates that better rate determinations, measured or calculated directly for H_2S rather than scaled from rates for H_2O, are likely to significantly improve the accuracy of radiative transfer models of H_2S.

Furthermore, as can be seen in the top two plots of Fig. 6, there is a more significant difference in the final integrated line intensity between the two molecular data files for the ($1_{1,0} \rightarrow 1_{0,1}$) line than for the ($3_{3,0} \rightarrow 3_{2,1}$) line, when considering the unscaled sets of collisional rates. This suggests that better detections of a wide variety of lines, i.e. those that vary significantly with the choice of collisional rates as well as those that do not, could help discriminate between choices of molecular data file. Since the biggest difference between the Gaussian abundance profiles for the best models with each of the two molecular data files was the e-folding radius, spatially resolved observations, such as those that can be performed with ALMA, will not only allow us to put better constraints on the H_2S distribution but also on the choice of molecular data file. Neither of these, however, is a full substitute for updated collisional rates calculated specifically for H_2S.

From the results tabulated in Table 5, it can be seen that the peak abundances required for the models to fit our observations did not change very significantly between the JHB and GS JHB molecular data files. However, there was a tendency for the ground state file to require larger abundances than the full file to reproduce the observed results. A similar effect was seen for NH_3 by Schöier et al. (2011) and Danilovich et al. (2014), although the effect is less pronounced for H_2S. These results do not conclusively justify the exclusion of the vibrationally excited states, although the choice of collisional rates does play a more significant role in altering the model results.

4.2. Choice of abundance distribution

The different abundance distributions used in our best-fit models are plotted in Fig. 4. There it can be seen that there are only minor differences between the abundance distributions resulting from the chemical models using the A and L parent molecules for a given molecular data file.

In the case of IK Tau and V1300 Aql, we had access to two o-H_2S detections from various telescopes. The two observed lines, ($1_{1,0} \rightarrow 1_{0,1}$) and ($3_{3,0} \rightarrow 3_{2,1}$), have reasonably separated emitting regions, with the lower-J line mostly emitting from the outer regions of the molecular envelope and the higher-J line emitting more strongly from the inner regions of the molecular envelope, as seen in the brightness distribution plots in Fig. 7. Hence, when fitting a Gaussian abundance distribution, we left the e-folding radius as a free parameter along with the peak abundance and constrained both with our observations. This led to large differences in radii between models using the LAMDA and JHB molecular data files, as seen in Fig. 4.

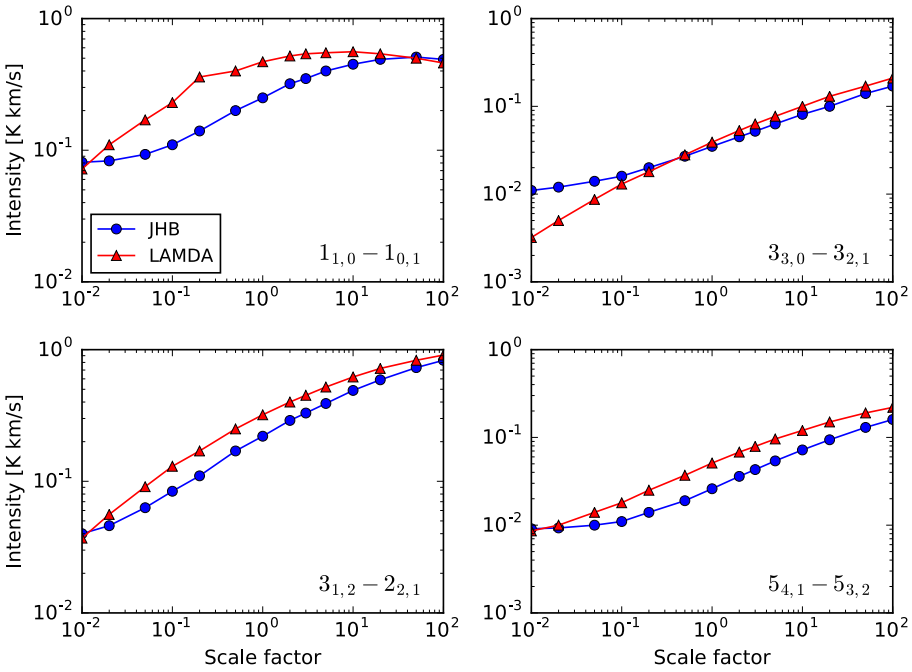

Fig. 6. Variation in integrated line intensities for four H_2S transition lines as a result of uniform scaling of the collisional rates given in the LAMDA and JHB molecular data files (see text for further details).

For the sources with only one detection, it is not possible to put any constraints on a Gaussian abundance profile, hence we did not include any such results in Table 5. The upper limit given by the non-detection for GX Mon adds some constraints, but not enough to give sufficient certainty. This is why we only include model results based on the abundance distributions generated by chemical modelling for GX Mon, WX Psc, and V1111 Oph.

The strongest emission lines in the frequency range accessible from APEX (and most ground-based telescopes) are those that we observed for this project and a few lines that fall in the ~400–500 GHz region. These higher frequency lines require long integration times to reach sufficiently good RMS noise levels to obtain clear detections due to several key H_2S lines falling in regions of poor atmospheric transmission, even in good weather conditions. Indeed, the p-H_2S ($1_{1,1} \rightarrow 0_{0,0}$) line, which is expected to be bright and would have provided an interesting point of comparison with the o-H_2S ($1_{1,0} \rightarrow 1_{0,1}$) line, lies at 452.390 GHz in the wing of a strong water vapour absorption feature at 448 GHz[8]. Observations in this region were unfortunately unsuitable for inclusion in the broad sulphur survey of which the present results are a part. However, now that we have some stars with clear H_2S detections, future targeted observations of the more accessible higher frequency H_2S lines would allow us to better constrain the H_2S emission in the observed AGB stars. The best and most reliable way to precisely constrain the abundance distribution of H_2S, especially in the absence of space-based observations, would be to use an interferometer that is capable of resolving the emitting region to observe a reliable H_2S line. When the Band 5 receiver (covering 157–212 GHz) is available for general observing, which is expected for ALMA Cycle 5 from early-2018, ALMA will have the capability to observe the H_2S ($1_{1,1} \rightarrow 0_{0,0}$) line at 168.763 GHz. The sizes of the H_2S emitting regions predicted by our models are of the order of a few arcseconds, depending on the source, which is well within the resolving capability of ALMA.

[8] This can be clearly seen using the APEX atmospheric transmission calculator at http://www.apex-telescope.org/sites/chajnantor/atmosphere/

4.3. Comparison with other studies

Previous observations of H_2S in AGB stars have mainly yielded detections towards OH/IR stars. Omont et al. (1993), for example, surveyed 34 sources and detected H_2S towards all seven OH/IR stars, four out of nine M-type AGB stars (other than the OH/IR stars), one out of three carbon AGB stars, and neither of the two S-type AGB stars. Our detection pattern is in general agreement with their results (see Fig. 1), aside from our exclusion of extreme OH/IR stars. Four of our five stars were also observed by Omont et al. (1993), who detected the same 168 GHz H_2S line in all four. Additionally, they found a weak detection of the 216 GHz H_2S line towards WX Psc, a line that was not observed as part of our survey.

Omont et al. (1993) also modelled the H_2S emission for WX Psc and OH 26.5 +0.6 including infrared rotational excitation. They find a high abundance of H_2S $\sim 1 \times 10^{-5}$ for both stars, accounting for a significant fraction of the sulphur budget, and their abundance distribution is a step function out to $\sim 10^{16}$ cm, similar in size to many of our models. Their calculated abundance for WX Psc is an order of magnitude larger than our models, although they do note the significant uncertainty in their model due to noisy observations. They also find that models with smaller radial distributions of H_2S yield implausibly large abundances, which is in agreement with our modelling results.

The earlier study of Ukita & Morris (1983) failed to detect H_2S in all but OH 231.8 +4.2, an extreme OH/IR star. Their source list includes lower mass-loss rate AGB stars (and some other types of objects) and there is little overlap with our source list, since they mainly observed northern sources and we mainly observed southern sources.

Yamamura et al. (2000) identified the sulphur-bearing molecule HS in R And, an S-type AGB star, using high resolution infrared spectra. These authors noted that HS is located in the stellar atmosphere and moves inwards during stellar pulsations. They did not simultaneously detect H_2S in their spectra. Since R And is a relatively low mass-loss rate S-type star ($\dot{M} = 5 \times 10^{-7}$ $M_\odot$ yr^{-1}; Danilovich et al. 2015), we would not expect to detect H_2S based on the survey results in this present study.

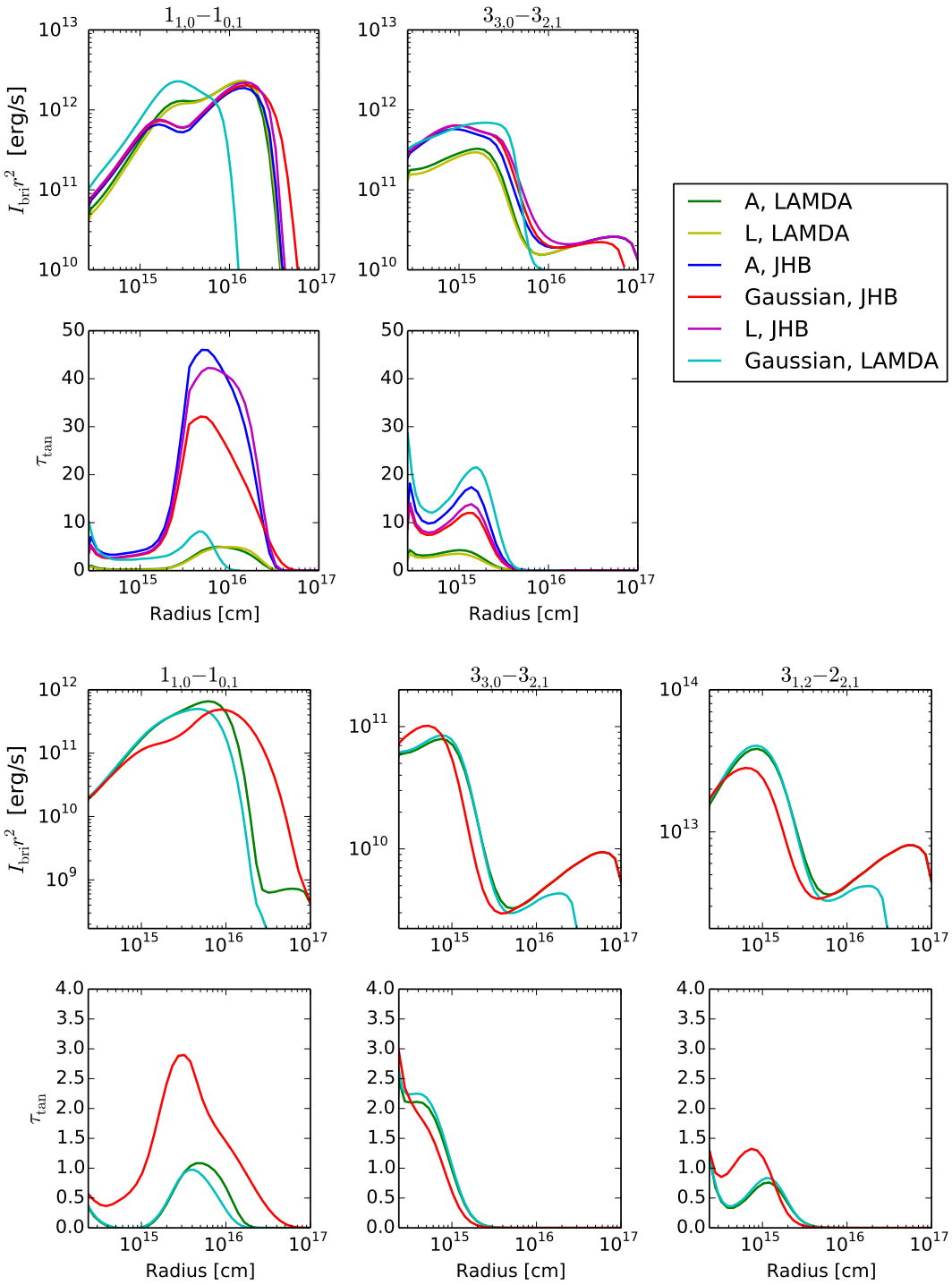

Fig. 7. Results from various model fits to o-H_2S for V1300 Aql (*top*) and IK Tau (*bottom*). Transition numbers at the top of a column indicate the line for which the parameters are plotted. The *top row* of the plot of each star shows the tangential brightness distribution of the emission line, $I_{\rm bri}$, scaled with the radius squared, r^2, to emphasise the features more clearly plotted against radius. The corresponding *bottom row* shows the tangential optical depth of the emission line with radius. The legend in the top right is given for V1300 Aql and also applies to the more sparsely selected lines for IK Tau.

4.4. Comparison with chemical models

The L and A abundance distributions from chemical model results used in our radiative transfer modelling were based on the parent species listed in the Li et al. (2016) and Agúndez et al. (2010) studies rather than on their direct results. For example, Li et al. (2016) based their models on the example of IK Tau specifically and assumed that the S-bearing parent species are H_2S, SO, SO_2, CS, and SiS. Their resultant radial distributions of these molecules start high at their inner radii (set to 10^{15} cm) and gradually decrease aside from a slight increase of H_2S, which can be seen in our Fig. 4. These authors found a much lower H_2S abundance than our radiative transfer results for IK Tau (and indeed, all five of our sources), which are a few orders of magnitude higher. The Li et al. (2016) results are also in disagreement with the observational SO results found by Danilovich et al. (2016) for IK Tau, which show a lower inner abundance of SO with a peak at $\sim 10^{16}$ cm.

The Agúndez et al. (2010) study covered a similar region of the CSE – beginning at 10^{14} cm, further inwards than Li et al. (2016) – but primarily focused on the effect of clumpiness in the CSE. Their S-bearing parent species for oxygen-rich CSEs are SiS, CS, and H_2S, with a much lower H_2S abundance, by at least two orders of magnitude, than we find in any of our models.

The models of Willacy & Millar (1997) examined a similar region of the CSE as those of Li et al. (2016) but assumed different parent molecules and corresponding initial abundances. Their parent molecules included SiS and H_2S, with a large initial abundance of H_2S that accounts for most of the sulphur in the CSE. These authors used TX Cam as their example star, which is not in our sample but is similar to IK Tau in terms of mass-loss rate. However, unlike our results for IK Tau, their resultant H_2S distribution is in close agreement with our Gaussian and JHB model for V1300 Aql in terms of both abundance and distribution size.

The chemical models of Gobrecht et al. (2016) primarily looked at the innermost regions of the CSE, within the dust condensation radius, and focus on shock-induced chemistry. Their model also used IK Tau as the exemplar source. Their initial abundances were based on thermal equilibrium calculations and they began with a high abundance of H_2S, accounting for most of the sulphur. This drops off within nine stellar radii to only $\sim 10^{-8}$, a few orders of magnitude lower than our models, which have inner radii close to the outer radius used by Gobrecht et al. (2016).

From the differences in the above models, especially those which examine a similar region of the CSE as our radiative transfer models, it is clear that a different choice of parent molecules and their abundances can change the abundance distributions predicted by the chemical models. Since we found a range of o-H_2S abundances among our sources, from 4×10^{-7} to 2.5×10^{-5}, it is also likely that different conditions (temperature, density, and possibly age) in different stars led to different abundances of various molecules such as H_2S. A goal of our ongoing work is to determine abundances for five key S-bearing molecules (H_2S, SO, SO_2, CS, and SiS) for a consistent sample of stars based on observations and radiative transfer modelling. These results can then be compared with chemical models *en masse* and, ideally, adjusting the chemical models to agree with these results will yield more precise chemical models that better represent individual AGB stars.

4.5. Trends, or lack there of, in H_2S abundance

V1300 Aql was found to have a higher H_2S abundance than the other four stars in our sample, especially when considering the models calculated using the JHB molecular data file and/or a Gaussian abundance distribution. The H_2S abundance is about an order of magnitude higher than that found for V1111 Oph, the source with the most similar mass-loss rate, and more than an order of magnitude higher than that found for WX Psc, the source with the largest mass-loss rate; this is a factor of four higher than the mass-loss rate of V1300 Aql. The most similar abundance and mass-loss rate combination we found was towards GX Mon, which has a slightly lower mass-loss rate than V1300 Aql, a slightly lower H_2S abundance, and a similar separation between abundances calculated from the JHB and LAMDA molecular data files. However, the GX Mon models are based primarily on only one H_2S detection, which is also noisier than the corresponding V1300 Aql transition, making those models slightly less certain.

There is no clear correlation between our modelled H_2S abundances, when looking at a single, consistent modelling method, and mass-loss rate or CSE density ($\dot{M}/\upsilon_\infty$). The clearest correlation between mass-loss rate and H_2S abundance is based on the fact that H_2S was only detected for the highest mass-loss rate stars, as shown in Fig. 1. As emphasised there, H_2S was not detected towards W Hya, which is a bright M-type star (with a similar brightness to V1111 Oph) that has a low mass-loss rate; this tentatively suggests that H_2S may only be present in higher mass-loss rate stars. Outside of the sample of stars examined here, the most significant group of AGB stars with H_2S detections are the high mass-loss rate extreme OH/IR stars, such as those from the studies of Ukita & Morris (1983), Omont et al. (1993), and Justtanont et al. (2015). Of the stars in our sample, none have been confirmed to be extreme OH/IR stars. Indeed, extreme OH/IR stars were excluded from our sulphur survey sample due to the difficulty in finding a certain circumstellar model from CO emission lines that are often rife with interstellar contamination.

Hashimoto & Izumiura (1997) suggested that V1300 Aql has recently become an OH/IR star in the superwind phase (Iben & Renzini 1983; Justtanont et al. 2013; de Vries et al. 2014), based on an analysis of the compact and thick circumstellar dust envelope. More recently, Cox et al. (2012) studied the extended dust emission of a large sample of AGB stars and reported V1300 Aql to have no extended emission that can be resolved at 70 or 160 μm by *Herschel*/PACS photometry, which supports the premise of a small dust envelope. Furthermore, Ramstedt & Olofsson (2014) found a low $^{12}CO/^{13}CO$ ratio of 7, suggesting that V1300 Aql has undergone hot bottom burning (Lattanzio & Wood 2003). Both the OH/IR phase and hot bottom burning occur at the end of the AGB phase, so the presence of one is suggestive of the other.

If V1300 Aql is indeed in the early stages of the superwind phase, this could explain why it has a higher H_2S abundance and hence that it should be grouped with the OH/IR stars in this respect. Although precise H_2S abundances are not presently know for extreme OH/IR stars, they are likely to be significant based on the intensity of various observations such as those by Omont et al. (1993), who detected the 168 GHz and 216 GHz H_2S lines in all their surveyed OH/IR stars and whose analysis suggests abundances of the order of $\sim 10^{-5}$.

There is not presently enough information to draw firm conclusions as to whether H_2S is more abundant in extreme OH/IR stars, let alone any explanations as to why that may be the case. Further investigation, as well as a more accurate molecular data file (see Sect. 4.1), will allow us to better constrain the occurrence of H_2S in AGB stars.

4.6. H_2S and ramifications for the sulphur budget

Our results indicate that for some oxygen-rich AGB stars with high mass-loss rates, H_2S may account for a significant fraction of the sulphur budget. This is in contrast with SO and SO_2, which were found by Danilovich et al. (2016) to be the most significant carriers of sulphur in low mass-loss rate oxygen-rich AGB stars. In carbon stars the most significant carriers of sulphur are CS and SiS (Olofsson et al. 1993; Schöier et al. 2007) with H_2S only playing a minor role, if any at all.

Since sulphur is not nucleosynthesised in AGB stars or their progenitors, we expect the overall sulphur abundance to match that of the solar neighbourhood, although with most of our sources at distances of 550–750 pc (except for IK Tau at 265 pc) this may not necessarily hold. However, Rudolph et al. (2006)

showed that while there is a trend for higher sulphur abundances towards the Galactic centre and lower abundances in the outer parts of the Galaxy, it is not a steep gradient and the approximate S/H_2 $\sim 2–3 \times 10^{-5}$ that can be derived from their results is likely to hold for all of our sources. We find a slight overabundance of H_2S in two of our V1300 Aql models (the Gaussian + LAMDA model and the L + ground state JHB model), which give slightly more H_2S than the expected abundance of sulphur allows. We have already discussed the likely over-prediction of H_2S due to the exclusion of excited vibrational states and these are likely a symptom of that issue. Our remaining models for all sources do not yield higher H_2S abundances than the expected sulphur abundance.

The only source for which the H_2S abundance is high enough to account for all of the sulphur is V1300 Aql, although for GX Mon H_2S also accounts for a significant portion of the sulphur. Indeed, applying an ortho-to-para ratio of 3 to our results in Table 5 pushes the abundances well into the expected S/H_2 range (or above, in the cases noted above). The ortho-to-para ratio of 3 comes from assuming statistical equilibrium (valid for warm formation temperatures) and, owing to the low quality of our only para-H_2S detection, is not a ratio we can confirm observationally or through modelling. The concern here is the possibility that other S-bearing molecules also have significant abundances and consequently push the derived total sulphur abundance above realistic levels. Our subsequent papers in this series will investigate the abundances of the other key sulphur molecules observed towards V1300 Aql and GX Mon in more detail, but a preliminary analysis of V1300 Aql gives peak SiS, SO, and SO_2 abundances of $\sim 1 \times 10^{-6}$ each, and a peak abundance of CS of $\sim 1 \times 10^{-7}$. This brings the total sulphur abundances to within the considerable uncertainties of the expected value and suggests that other molecules such as HS and atomic S are likely to play, at most, only a minor role in the circumstellar envelope of V1300 Aql.

5. Conclusions

In this study, we present new H_2S observations acquired as part of a larger APEX survey of sulphur-bearing molecules in the circumstellar envelopes of AGB stars. Our clearest detections are of the 168.763 GHz o-H_2S ($1_{1,0} \rightarrow 1_{0,1}$) line, which is the main focus of our subsequent analysis. We also tentatively detect the equivalent o-$H_2{}^{34}S$ line and one p-H_2S line. In addition to the five sources with detected H_2S lines, we present a comprehensive series of non-detections with sensitive RMS limits for a further 16 stars of various chemical types and a range of mass-loss rates.

We perform detailed radiative transfer models of o-H_2S for all five detected sources, using two abundance distributions based on the results of chemical models and, where a second o-H_2S line is detected, using a Gaussian distribution profile. For each model we use three different molecular data files, mostly differing in their choices of collisional de-excitation rates, which were scaled from different calculations of H_2O collisional rates. We find a spread of peak abundances of o-H_2S ranging from $\sim 4 \times 10^{-7}$ to 3×10^{-5}, depending on the source and modelling method used. Overall, we determine that H_2S can account for a significant fraction of the overall sulphur budget, and we find it to be the dominant S-bearing molecule in V1300 Aql and GX Mon in particular.

Because we have, at most, only one detection of p-H_2S or o-$H_2{}^{34}S$ for each source, we did not model these two species. It is not possible to make accurate comparisons of abundances or isotopologue ratios without full radiative transfer models because some the lines in question, and certainly the o-$H_2{}^{32}S$ lines under comparison, are optically thick. This will only be possible in the future if we can obtain more observations to allow for more constrained models of these species. Alternatively, more certain o-H_2S models with updated calculations of collisional rates will also allow for better constraints on H_2S in general and hence its isotopologues and spin isomers.

Acknowledgements. The authors would like to acknowledge John H. Black for his compilation of the H_2S molecular data file used in our modelling. L.D. and T.D. acknowledge support from the ERC consolidator grant 646758 AEROSOL and the FWO Research Project grant G024112N. M.V.d.S. and L.D. acknowledge support from the Research Council of the KU Leuven under grant number GOA/2013/012. T.J.M. acknowledges support from the STFC, grant reference ST/P000312/1. Based on observations made with APEX under programme IDs O-097.F-9318 and O-098.F-9305. APEX is a collaboration between the Max-Planck-Institut für Radioastronomie, the European Southern Observatory, and the Onsala Space Observatory. HIFI has been designed and built by a consortium of institutes and university departments from across Europe, Canada and the United States under the leadership of SRON Netherlands Institute for Space Research, Groningen, The Netherlands and with major contributions from Germany, France and the US Consortium members are: Canada: CSA, U. Waterloo; France: CESR, LAB, LERMA, IRAM; Germany: KOSMA, MPIfR, MPS; Ireland, NUI Maynooth; Italy: ASI, IFSI-INAF, Osservatorio Astrofisico di Arcetri-NAF; The Netherlands: SRON, TUD; Poland: CAMK, CBK; Spain: Observatorio Astronómico Nacional (IGN), Centro de Astrobiología (CSIC-INTA). Sweden: Chalmers University of Technology – MC2, RSS & GARD; Onsala Space Observatory; Swedish National Space Board, Stockholm University – Stockholm Observatory; Switzerland: ETH Zurich, FHNW; USA: Caltech, JPL, NHSC.

References

Agúndez, M., Cernicharo, J., & Guélin, M. 2010, ApJ, 724, L133
Begemann, B., Dorschner, J., Henning, T., Mutschke, H., & Thamm, E. 1994, ApJ, 423, L71
Billade, B., Nystrom, O., Meledin, D., et al. 2012, IEEE Trans. Terahertz Sci. Technol., 2, 208
Bujarrabal, V., Hifistars, & Success Teams 2011, in Why Galaxies Care about AGB Stars II: Shining Examples and Common Inhabitants, eds. F. Kerschbaum, T. Lebzelter, & R. F. Wing, ASP Conf. Ser., 445, 577
Cernicharo, J., Kahane, C., Guelin, M., & Hein, H. 1987, A&A, 181, L9
Cernicharo, J., Guélin, M., & Kahane, C. 2000, A&AS, 142, 181
Cherchneff, I. 2006, A&A, 456, 1001
Cherchneff, I. 2012, A&A, 545, A12
Cordiner, M. A., & Millar, T. J. 2009, ApJ, 697, 68
Cox, N. L. J., Kerschbaum, F., van Marle, A.-J., et al. 2012, A&A, 537, A35
Daniel, F., Dubernet, M.-L., Pacaud, F., & Grosjean, A. 2010, A&A, 517, A13
Daniel, F., Dubernet, M.-L., & Grosjean, A. 2011, A&A, 536, A76
Danilovich, T., Bergman, P., Justtanont, K., et al. 2014, A&A, 569, A76
Danilovich, T., Teyssier, D., Justtanont, K., et al. 2015, A&A, 581, A60
Danilovich, T., De Beck, E., Black, J. H., Olofsson, H., & Justtanont, K. 2016, A&A, 588, A119
De Beck, E., Kamiński, T., Patel, N. A., et al. 2013, A&A, 558, A132
de Graauw, T., Helmich, F. P., Phillips, T. G., et al. 2010, A&A, 518, L6
de Vries, B. L., Blommaert, J. A. D. L., Waters, L. B. F. M., et al. 2014, A&A, 561, A75
Dubernet, M.-L., Daniel, F., Grosjean, A., et al. 2006, A&A, 460, 323
Dubernet, M.-L., Daniel, F., Grosjean, A., & Lin, C. Y. 2009, A&A, 497, 911
Faure, A., & Josselin, E. 2008, A&A, 492, 257
Faure, A., Crimier, N., Ceccarelli, C., et al. 2007, A&A, 472, 1029
Gobrecht, D., Cherchneff, I., Sarangi, A., Plane, J. M. C., & Bromley, S. T. 2016, A&A, 585, A6
Goebel, J. H., & Moseley, S. H. 1985, ApJ, 290, L35
Green, S., Maluendes, S., & McLean, A. D. 1993, ApJS, 85, 181
Güsten, R., Nyman, L. Å., Schilke, P., et al. 2006, A&A, 454, L13
Hashimoto, O., & Izumiura, H. 1997, Ap&SS, 251, 207
Iben, Jr., I., & Renzini, A. 1983, ARA&A, 21, 271
Immer, K., Belitsky, V., Olberg, M., et al. 2016, The Messenger, 165, 13
Justtanont, K., Khouri, T., Maercker, M., et al. 2012, A&A, 537, A144
Justtanont, K., Teyssier, D., Barlow, M. J., et al. 2013, A&A, 556, A101
Justtanont, K., Barlow, M. J., Blommaert, J., et al. 2015, A&A, 578, A115
Khouri, T., de Koter, A., Decin, L., et al. 2014, A&A, 561, A5
Lattanzio, J. C., & Wood, P. R. 2003, in Asymptotic Giant Branch Stars (Springer), 23
Li, X., Millar, T. J., Heays, A. N., et al. 2016, A&A, 588, A4

Lide, D. 2003, CRC Handbook of Chemistry and Physics, 84th edn. (Taylor & Francis)
Lindqvist, M., Nyman, L.-A., Olofsson, H., & Winnberg, A. 1988, A&A, 205, L15
Maercker, M., Schöier, F. L., Olofsson, H., Bergman, P., & Ramstedt, S. 2008, A&A, 479, 779
Maercker, M., Danilovich, T., Olofsson, H., et al. 2016, A&A, 591, A44
McElroy, D., Walsh, C., Markwick, A. J., et al. 2013, A&A, 550, A36
Millar, T. J., Herbst, E., & Bettens, R. P. A. 2000, MNRAS, 316, 195
Olofsson, H., Eriksson, K., Gustafsson, B., & Carlstroem, U. 1993, ApJS, 87, 305
Omont, A., Lucas, R., Morris, M., & Guilloteau, S. 1993, A&A, 267, 490
Ott, S. 2010, in Astronomical Data Analysis Software and Systems XIX, eds. Y. Mizumoto, K.-I. Morita, & M. Ohishi, ASP Conf. Ser., 434, 139
Patel, N. A., Young, K. H., Gottlieb, C. A., et al. 2011, ApJS, 193, 17
Pickett, H. M., Poynter, R. L., Cohen, E. A., et al. 1998, J. Quant. Spectr. Rad. Transf., 60, 883
Ramstedt, S., & Olofsson, H. 2014, A&A, 566, A145
Ramstedt, S., Schöier, F. L., Olofsson, H., & Lundgren, A. A. 2008, A&A, 487, 645
Reyniers, M., & van Winckel, H. 2007, A&A, 463, L1
Risacher, C., Vassilev, V., Monje, R., et al. 2006, A&A, 454, L17
Roelfsema, P. R., Helmich, F. P., Teyssier, D., et al. 2012, A&A, 537, A17
Rothman, L. S., Gordon, I. E., Barbe, A., et al. 2009, J. Quant. Spectr. Rad. Transf., 110, 533
Rudolph, A. L., Fich, M., Bell, G. R., et al. 2006, ApJS, 162, 346
Schöier, F. L., & Olofsson, H. 2001, A&A, 368, 969
Schöier, F. L., van der Tak, F. F. S., van Dishoeck, E. F., & Black, J. H. 2005, A&A, 432, 369
Schöier, F. L., Bast, J., Olofsson, H., & Lindqvist, M. 2007, A&A, 473, 871
Schöier, F. L., Maercker, M., Justtanont, K., et al. 2011, A&A, 530, A83
Schöier, F. L., Ramstedt, S., Olofsson, H., et al. 2013, A&A, 550, A78
Tenenbaum, E. D., Dodd, J. L., Milam, S. N., Woolf, N. J., & Ziurys, L. M. 2010, ApJS, 190, 348
Ukita, N., & Morris, M. 1983, A&A, 121, 15
van der Tak, F. 2011, in The Molecular Universe, eds. J. Cernicharo, & R. Bachiller, IAU Symp., 280, 449
Vassilev, V., Meledin, D., Lapkin, I., et al. 2008, A&A, 490, 1157
Viswanathan, R., & Dyke, T. R. 1984, J. Mol. Spectr., 103, 231
Waelkens, C., Van Winckel, H., Bogaert, E., & Trams, N. R. 1991, A&A, 251, 495
Willacy, K., & Millar, T. J. 1997, A&A, 324, 237
Yamamura, I., Kawaguchi, K., & Ridgway, S. T. 2000, ApJ, 528, L33
Zhang, K., Jiang, B. W., & Li, A. 2009, ApJ, 702, 680